J Mater Sci (2013) 48:3870–3876
DOI 10.1007/s10853-013-7189-9

Graphene-encapsulated mesoporous SnO_2 composites as high performance anodes for lithium-ion batteries

Shuhua Jiang · Wenbo Yue · Ziqi Gao ·
Yu Ren · Hui Ma · Xinhua Zhao · Yunling Liu ·
Xiaojing Yang

Received: 11 November 2012 / Accepted: 22 January 2013 / Published online: 6 February 2013

Abstract Mesoporous metal oxides such as SnO_2 exhibit a superior electrochemical performance as anode materials for lithium-ion batteries due to their large surface areas and uniform pores. However, they suffer from the capacity fading in varying degrees during cycles because their partial pores may collapse during the charge–discharge process. Herein, graphene-encapsulated mesoporous SnO_2 composites have been simply synthesized using a modified stepwise heterocoagulation method. These graphene-based SnO_2 composites exhibit not only higher capacities and better rate capabilities but also improved cycle performances, suggesting that the electrochemical performance of mesoporous SnO_2 can be further enhanced by graphene encapsulation.

Introduction

Lithium-ion batteries (LIBs) have been widely used in portable electronic devices (e.g., cell phones, laptop computers) due to their superior properties such as high energy density, long cycle life, no memory effect, and environmental friendliness. Many metal oxides are used as anode materials for LIBs due to their high theoretic capacities and low cost. For instance, SnO_2 has a high theoretic capacity of 782 mA h g^{-1}, much higher than that of the commonly used LiC_6 anodes (370 mA h g^{-1}) [1]. However, many metal oxides show rapid capacity fading and poor cycling behaviors because of the dramatic volume change during the charge–discharge process. Some methods have been adopted to alleviate the volume changes and improve the cycling stability for these metal oxides. One of them is to decrease the size of SnO_2 particles into the nanoscale (e.g., nanowire, nanorod), which can shorten the lithium-ion diffusion pathway and improve its rate capacity [2, 3]. Another method is to make a metal oxide composite with carbon, which can effectively buffer the strain from the volume change of metal oxides during the charge–discharge process and maintain the high electrical conductivity of the electrode. For instance, the carbon-coated SnO_2 composites were prepared through a carbonization approach and showed an outstanding high-rate cycling performance [4–6]. Moreover, the electrochemical performance of porous activated carbon-containing SnO_2 can be further enhanced by additional carbon coating [7]. On the other hand, in situ growth of SnO_2 on the carbon substrate (e.g., carbon nanotube) can also improve its electrochemical performance [8]. Recently, a novel two-dimensional carbon matrix, graphene, has been prepared and exhibits superior properties such as high electrical conductivities, unique mechanical properties, and large surface areas

---

Electronic supplementary material The online version of this article (doi:10.1007/s10853-013-7189-9) contains supplementary material, which is available to authorized users.

S. Jiang · W. Yue · Z. Gao · H. Ma · X. Zhao · X. Yang (✉)
Beijing Key Laboratory of Energy Conversion and Storage Materials, College of Chemistry, Beijing Normal University, Beijing 100875, People's Republic of China
e-mail: yang.xiaojing@bnu.edu.cn

W. Yue (✉)
College of Chemistry, Beijing Normal University, 19 Xinjiekou Wai Street, Beijing 100875, People's Republic of China
e-mail: wbyue@bnu.edu.cn

Y. Ren
National Institute of Clean-and-low-carbon Energy, Beijing 102209, People's Republic of China

Y. Liu
State Key Laboratory of Inorganic Synthesis and Preparative Chemistry, College of Chemistry, Jilin University, Changchun 130012, People's Republic of China

[9–12]. Therefore, compared to carbon-coated SnO_2, graphene-encapsulated SnO_2 is expected to exhibit enhanced electrochemical properties due to the superior properties of graphene. Graphene-based SnO_2 composites have been prepared by the in situ growth of SnO_2 particles on the surface of graphene and exhibit high reversible capacities and enhanced cycle performances [13–15]. Graphene-encapsulated metal oxides are another type of graphene-based composites, which are prepared by coassembly between negatively charged graphene oxide (GO) and positively charged oxide nanoparticles [16, 17].

Meanwhile, mesoporous metal oxides such as novel nanostructured materials not only deliver high charge–discharge capacities due to their large surface areas but also exhibit better cycle performance and rate capabilities because the mesopores may act as a volume buffer capable of accepting the volume expansion associated to conversion reactions and protect the electrode from pulverization [18–21]. Recently, it is reported that SnO_2 particles with a mesoporous structure exhibit enhanced electrochemical properties in comparison with its bulk counterpart [22–24]. However, the capacity fading still occurs after several cycles because the partial pore structures may collapse during the charge–discharge process. To solve this problem, graphene-based mesoporous metal oxides such as graphene-encapsulated mesoporous SnO_2 were developed [25, 26], which should exhibit further enhanced electrochemical performance.

A core-shell particle can be synthesized by depositing many cationic small particles onto an anionic large particle, namely the stepwise heterocoagulation method [27, 28]. The negatively charged GO at high pH (>7) can be regarded as an anionic large particle and the positively charged mesoporous SnO_2 particles (M-SnO_2) at low pH (<4) can be regarded as cationic small particles. Therefore, graphene-encapsulated SnO_2 particles can be simply prepared through electrostatic interactions and reduction of GO with reducing agents such as hydrazine or L-ascorbic acid (VC) [29, 30]. Herein, we describe a facile strategy for the preparation of graphene-encapsulated M-SnO_2 by a stepwise heterocoagulation method. These novel electrodes exhibit higher capacities, higher rate capabilities, and better cycle performances in comparison with bare mesoporous SnO_2 particles.

Experimental section

Syntheses of graphene-encapsulated mesoporous SnO_2 composites

Mesoporous SnO_2 and GOs were synthesized according to the published literature (see supporting information) [31, 32]. The graphene-encapsulated mesoporous SnO_2 composites were synthesized by coassembly between positively charged M-SnO_2 and negatively charged GO, and reduction of GO with VC. In a typical process, 0.15 g of M-SnO_2 powders and 0.03 or 0.05 g of GO were dispersed in 50 and 200 mL distilled water, respectively. The pH of M-SnO_2 suspension was adjusted to 2–3 by hydrochloride acid and the pH of GO suspension was adjusted to 7–8 by aqueous ammonia. Subsequently, M-SnO_2 suspension was added into GO suspension under mild magnetic stirring. After 1 h, 0.40 g of VC was added into the above suspension under nitrogen atmosphere to reduce GO to graphene. After 24 h, the graphene-encapsulated M-SnO_2 particles were collected by centrifugation, washed with distilled water thrice, and dried at 313 K. The mesoporous SnO_2 prepared by SBA-15 and KIT-6 as templates was denoted as M-SnO_2(S) and M-SnO_2(K), and the corresponding graphene composites were denoted as GM-SnO_2(S) and GM-SnO_2(K), respectively.

Analytical methods

Specimens were initially characterized by XRD on a Phillips X'pert Pro MPD diffractometer with Cu K_α radiation. A Quantachrome NOVA 2000e sorption analyzer was used to examine the N_2 adsorption and desorption properties of specimens at liquid nitrogen temperature (77 K). The samples were degassed at 423 K overnight prior to the measurement. The Fourier transform infrared (FT-IR) spectra were recorded on a Nicolet-380 Fourier transform infrared spectrometer in the range of 400–4000 cm^{-1} and X-ray photoelectron (XPS) spectra were recorded on a Shimadzu Axis Ultra spectrometer with an Mg $K_\alpha = 1253.6$ eV excitation source. Further characterization was performed by high-resolution transmission electron microscopy (HRTEM) on a JEOL JEM-2010 electron microscope operated at 200 kV and scanning electron microscopy (SEM) on a JEOL JSM-6700F electron microscope at an accelerating voltage of 1 kV.

Electrochemical testing

For electrochemical characterization, the composite electrodes were fabricated by mixing the active materials, acetylene black, and polyvinylidene difluoride (PVDF) dissolved in *N*-methyl-2-pyrrolidine (NMP) in a weight ratio of 70:15:15. The mixed slurry was pressed onto a copper foil and dried at 383 K in vacuum for 24 h. Cell assembly was carried out in an Ar-filled glove box. The electrolyte was 1 M solution of $LiPF_6$ in EC:DEC:DMC with volume ratio 1:1:1. Electrochemical performances were measured with a CR2032-type coin cell with lithium metal as the negative electrode. The galvanostatic charge–discharge performance was measured with a LAND test system at room temperature, and the voltage range was from 0.01 to 2.0 V (versus Li/Li^+),

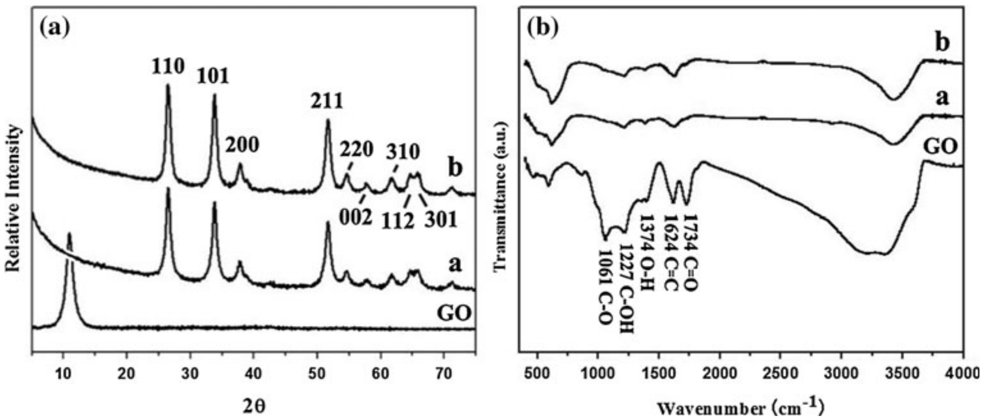

Fig. 1 XRD patterns and FT-IR spectra of GO, GM-SnO_2(S) (**A**) and GM-SnO_2(K) (**B**)

with a constant current of 0.1–1C (1C = 782 mA g^{-1}). Cyclic voltammetry (CV) tests were performed between 0.01 and 2.5 V with a scan rate of 0.2 mV s^{-1}, and electrochemical impedance spectroscopy (EIS) was carried out in the frequency range from 100 kHz to 10 mHz on a Princeron PSTAT 4000 electrochemical station.

Results and discussion

Materials characterization

Firstly, two kinds of mesoporous SnO_2 were synthesized using SBA-15 and KIT-6 as the templates. The N_2 adsorption desorption isotherms of two specimens in Fig. S1A show type IV curves with a hysteresis loop, indicative of the mesostructural feature. The surface area of M-SnO_2(K) is 98.7 m^2 g^{-1}, which is larger than that of the M-SnO_2(S) samples (88.4 m^2 g^{-1}). Fig. S1B shows the derived pore size distributions and indicates that these porous materials contain ca. 3.5 nm diameter pores. The mesostructures of M-SnO_2(S) and M-SnO_2(K) samples were also observed by TEM (Fig. S1C and D). The SBA-15- and KIT-6-templated SnO_2 particles have a hexagonal and cubic porous structure, respectively. Subsequently, these mesoporous SnO_2 particles were encapsulated by graphene nanosheets for enhanced electrode performance. Fig. 1A shows the XRD patterns of GO, GM-SnO_2(S) and GM-SnO_2(K) samples. Only one peak centered at ca. 10.9° can be observed for GO, corresponding to a basal spacing of 8.1 Å, whereas it disappears in the XRD patterns of GM-SnO_2(S) and GM-SnO_2(K) specimens. It may be implied that GO was reduced to graphene in the presence of VC. Besides, the conventional stacking peak of graphene nanosheets at ca. 26° is also not detected, which may be ascribed to the formation of graphene-encapsulated mesoporous particles. On the other hand, these characteristic peaks in XRD patterns (Fig. 1A, a and b) can be indexed to the SnO_2 structure (group space $P4_2$/mnm), indicating that SnO_2 particles were not reduced by VC. Figure 1B shows the FT-IR spectra of GO, GM-SnO_2(S) and GM-SnO_2(K) samples. In the FT-IR spectrum of GO, the absorption bands at 1734, 1374, 1227, 1061, and 1624 cm^{-1} correspond to the stretching vibration of C=O (carboxyl or carbonyl), O–H (carboxyl or intercalated water), C–OH (hydroxyl), C–O (epoxy or alkoxy), and the skeletal vibration of C=C from unoxidized graphitic domains [33, 34], whereas only C=C, O–H, and C–OH bands can be detected in the FT-IR spectra of GM-SnO_2(S) and GM-SnO_2(K). Moreover, the intensities of O–H and C–OH bands are much weaker than those of the corresponding bands for GO, suggesting that GO was definitely reduced by VC. The absorption band at ca. 621 cm^{-1} (Fig. 1B, a and b) can be assigned to the vibration of Sn–O–Sn [33, 34], confirming the presence of SnO_2 in composites.

The generated graphene was further confirmed by X-ray photoelectron spectroscopies (XPS). Figure 2 shows the XPS spectrum of GM-SnO_2(S) including the fine spectra of C 1s and Sn 3d. The peaks located at 284.6, 487.2, 495.5, and 531.2 eV can be assigned to the binding energy of C 1s, Sn $3d_{5/2}$, Sn $3d_{3/2}$, and O 1s, respectively, revealing the presence of C, O, and Sn elements [35, 36]. Furthermore, four peaks centered at 284.6, 286.6, 287.6, and 288.8 eV were detected in the fine spectrum of C 1 s, which correspond to the C–C (sp^2 C), C–O, C=O, and O–C=O groups. It is obvious that the oxygen-containing functional groups on the surfaces of the GO were almost removed according to the relative intensities of these peaks. The XPS result shows that the as-synthesized sample consisted of graphene and SnO_2 particles, which is consistent with the XRD and FT-IR results.

The morphology and structure of GM-SnO_2(S) and GM-SnO_2(K) specimens were elucidated by SEM and TEM. According to the SEM images of GM-SnO_2(S) and GM-SnO_2(K) specimens (Fig. 3a and b), the mesoporous SnO_2 particles were encapsulated by the transparent and wrinkled graphene nanosheets, though some porous particles are not coated effectively. Furthermore, some SnO_2 particles still congregate together, which may affect their electrochemical performance. An increase in the mass ratio

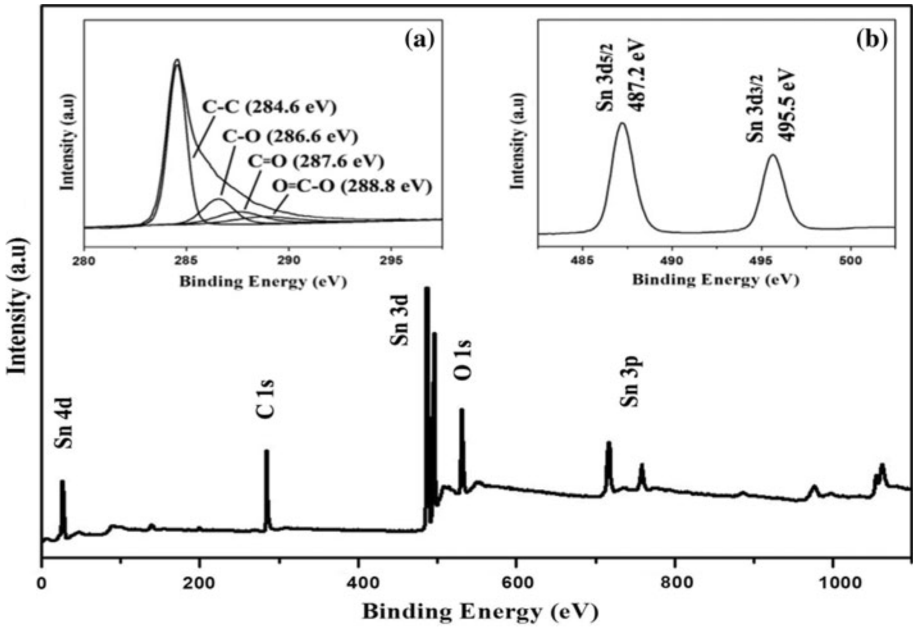

Fig. 2 XPS spectrum of GM-SnO$_2$(S). The insets are the fine spectra of C 1 s (**a**) and Sn 3d (**b**)

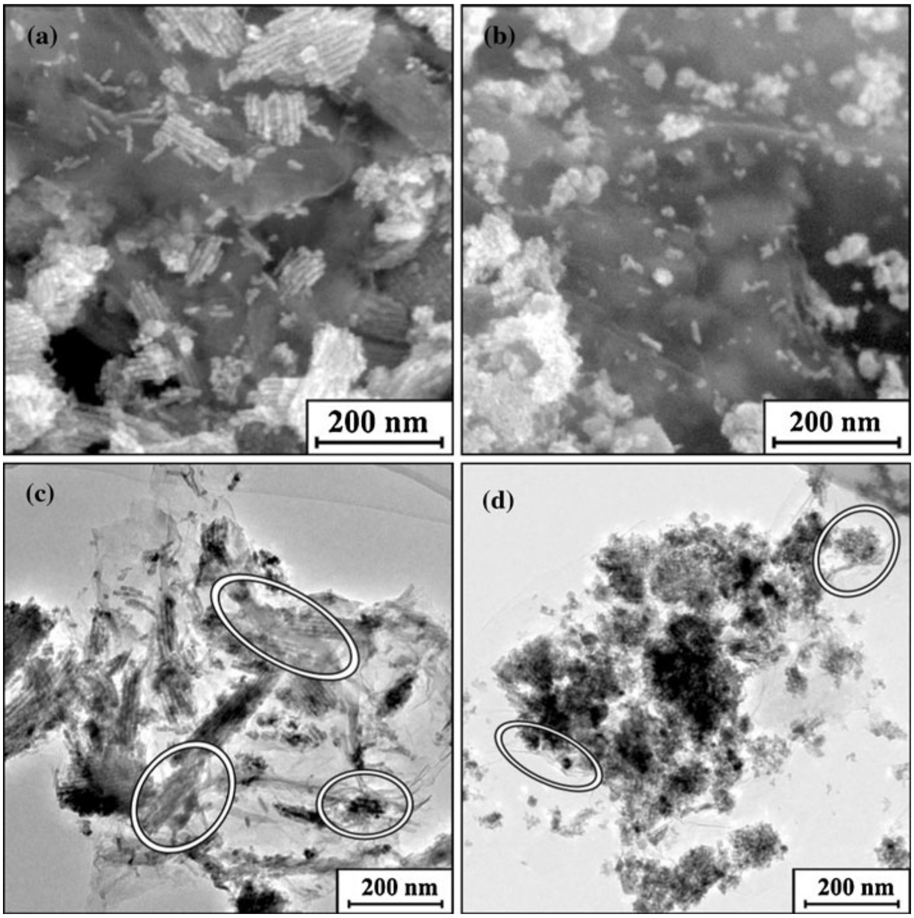

Fig. 3 SEM images and TEM images of GM-SnO$_2$(S) (**a**, **c**) and GM-SnO$_2$(K) (**b**, **d**)

of graphene to M-SnO$_2$ may be an alternative approach to reduce the number of uncoated SnO$_2$ particles and alleviate the aggregation. Figure S2 shows the SEM images of graphene-encapsulated M-SnO$_2$ containing large quantity of graphene, assigned to GM-SnO$_2$(S)-L and GM-SnO$_2$(K)-L. In brief, the mass ratio of graphene to M-SnO$_2$ is 1:5 for the

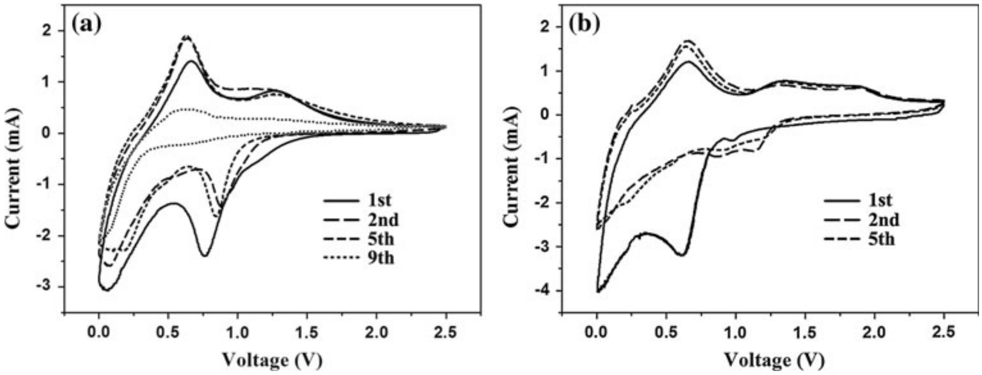

Fig. 4 Cyclic voltammograms of **a**, M-SnO_2(S) and **b**, GM-SnO_2(S) between 0.01 and 2.5 V with a scan rate of 0.2 mV s^{-1}

GM-SnO_2 sample and 1:3 for the GM-SnO_2-L sample. A small number of uncoated particles can be observed and the influence needs to be further verified by electrochemical testing. Figure 3c and d presents the TEM images of GM-SnO_2(S) and GM-SnO_2(K) specimens, respectively. The mesoporous particles and the wrinkled, transparent graphene nanosheets were distinctly observed in the TEM images. Moreover, the porous particles were well dispersed and strongly attached onto the surface of graphene nanosheets, and some of them were totally or partially encapsulated by graphene (see the white cycles in TEM images). Figure S3 shows the high-resolution TEM image of GM-SnO_2(S), and 2–3 layer graphene nanosheets with a lattice spacing of 0.341 nm were found at the edges, further confirming the core-shell structure and the complete reduction of GO [37]. These novel graphene-based composites should exhibit a better electrochemical performance than the uncoated particles.

Electrochemical testing

To identify the electrochemical reactions during cycles, cyclic voltammograms (CV) of M-SnO_2 and GM-SnO_2 electrodes were characterized in the range of 0.01–2.5 V. Figure 4a shows the CV profiles of M-SnO_2 in the 1st, 2nd, 5th, and 9th scanning cycles. In the first cathodic sweep, two distinct reduction peaks appear at 0.76 and 0.07 V. The former peak could be assigned to the transformation of $SnO_2 + Li^+$ to $Sn + Li_2O$ and the formation of a solid electrolyte interface (SEI). The latter peak could be attributed to the formation of Li_xSn alloy [4, 5, 8]. In the first anodic sweep, the two peaks observed at 0.66 and 1.26 V indicated the corresponding reversible reaction. The conversion of SnO_2 to Sn still occurs until the ninth cycle, which may result in large irreversible capacity. Figure 4b shows the 1st, 2nd, and 5th CV curves of GM-SnO_2 and in contrast, three pairs of current peaks can be observed at the potential of (0.98, 1.9 V), (0.64, 1.36 V), and (0.02, 0.65 V) in the first scanning cycle, indicating the conversions of SnO_2 to SnO, SnO_2 (or SnO) to Sn, and Sn to Li_xSn, respectively [13, 14]. Similarly, the peaks corresponding to the transformation of SnO_2 or SnO to Sn nearly disappeared after five cycles. Compared to the uncoated M-SnO_2, it seems that the graphene-encapsulated M-SnO_2 has a more stable structure during cycles.

The battery capacities and cycle performances of M-SnO_2(S), M-SnO_2(K), and the corresponding graphene-based composites were evaluated by galvanostatic measurements at a current density of 0.1C (ca. 78 mA g^{-1}). Figure S4 show the first and second cycle charge–discharge voltage profiles for these six samples. The curves are similar to the previous reports, indicating the same electrochemical pathway [33, 34, 38]. The first discharge capacities of M-SnO_2(S), M-SnO_2(K), GM-SnO_2(S), GM-SnO_2(K), GM-SnO_2(S)-L, and GM-SnO_2(K)-L are ca. 1155.1, 1262.0, 1309.3, 1563.6, 1218.3, and 1425.8 mA h g^{-1}, respectively. Compared to SBA-15-templated M-SnO_2, KIT-6-templated M-SnO_2 has a much higher surface area, leading to a higher capacity. On the other hand, graphene-encapsulated M-SnO_2 delivered higher capacities than the uncoated M-SnO_2, possibly resulting from the high electrical conductivity of graphene nanosheets between M-SnO_2 particles. It is worthwhile noting that the first discharge capacity of GM-SnO_2-L is slightly lower than that of GM-SnO_2 whatever template was used, implying that the further increase in the amount of graphene is not beneficial to the electrode capacity. It may be attributed to the lower theoretical capacity of graphene in comparison to that of SnO_2. Figure 5a and b shows the cycle performances of these six samples at the current density of 0.1C. It is also striking to note that graphene-encapsulated M-SnO_2 exhibited better cycle performances compared to bare M-SnO_2. Moreover, the cycle performance can be further improved with the increase of graphene content. The enhanced cycle performances can be attributed to the graphene layers, which may restrain the huge volume change and stabilize the mesostructure of M-SnO_2 during cycles. Figure 5c and d presents the cycle performances of these six samples measured at the current density from 0.1 to 1C. Although all capacities decreased

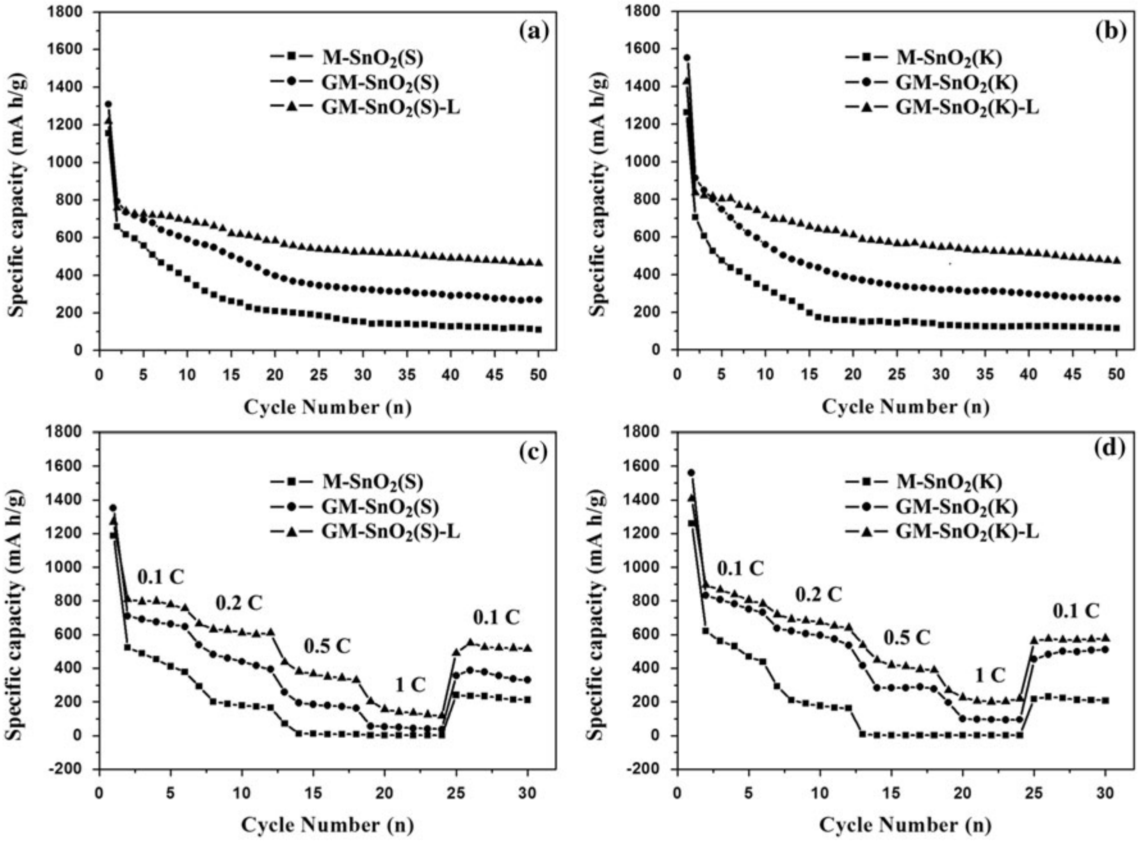

Fig. 5 The discharge capacities as a function of cycle numbers for M-SnO_2(S), M-SnO_2(K), GM-SnO_2(S), GM-SnO_2(K), GM-SnO_2(S)-L, and GM-SnO_2(K)-L samples at (**a**, **b**) 0.1C and (**c**, **d**) 0.1–1C

with the increase of the current density, the graphene-encapsulated M-SnO_2 samples still show higher reversible capacities, even at a high current density of ~780 mA g^{-1}. Additionally, after the high-rate measurements, the specific capacities of graphene-contained samples recovered to the high value when measured at 0.1C, indicating good cycling stability. Similarly, the rate capability of GM-SnO_2 is also enhanced with the increase of graphene content. As a result, the electrochemical property of mesoporous SnO_2 can be further improved by graphene encapsulation though it has exhibited better performance than bulk materials.

It was reported previously that SnO_2 particles tended to aggregate into Sn clusters during cycling, leading to large volume variation and capacity fading, while the dispersed SnO_2 on the graphene surface provided free space to accommodate the volume expansion [14, 39]. Thus, the morphology and structure of M-SnO_2 and GM-SnO_2 after 50 cycles were observed by TEM. No obvious mesostructure can be found in the TEM image of M-SnO_2 (Fig. S5A), implying the collapse of the mesoporous structure and aggregation of Sn particles during cycles. Although the porous structure derived from ordered nanorod arrays also disappeared in the TEM image of GM-SnO_2 (Fig. S5B), some mesopores were still present in Sn agglomeration and they are well dispersed by graphene nanosheets, which partly demonstrated the structural stability and resulted in better cycle performance. The electrochemical impedance spectra (EIS) studies of M-SnO_2 and GM-SnO_2 (Fig. S6) were also performed to evaluate the resistance against electron transfer during cycles. The measured impedance data were analyzed using the equivalent circuit (the inset of Fig. S6), and the symbols of Rs, Rct, Cd, and Zw denoted the solution resistance, charge transfer resistance, double layer capacitance, and Warburg impedance, respectively [39, 40]. The Nyquist plot of either M-SnO_2 or GM-SnO_2 shows a semicircle in the high frequency range and a sloping straight line in the low frequency range. The radius of the semicircles of the GM-SnO_2 electrode is smaller than that of the pure M-SnO_2 electrode, which may be attributed to the faster transfer rate of Li^+ ions in GM-SnO_2 because of the excellent conductivity of graphene. The significantly enhanced conductivity and stable structure of GM-SnO_2 may contribute to the enhanced performance in LIBs.

Conclusions

In conclusion, the graphene-encapsulated mesoporous SnO_2 composites as advanced anodes for LIBs were synthesized using a facile modified stepwise heterocoagulation method. The generated graphene was confirmed by XRD, FT-IR, and XPS, and the core-shell structure of the composite was confirmed by SEM and TEM. Compared to the pristine mesoporous SnO_2, the graphene-encapsulated one exhibited improved electrochemical performance, including higher capacities, higher rate capabilities, and better cycle performances. Additionally, the cycle performance and rate capability can be further improved by enlarging the content of graphene, though the reversible capacity may be slightly decreased at the initial cycles. Thus, it is an alternative method for mesoporous anodes to alleviate the capacity fading caused by collapsed pore structures during cycles. This simple synthetic method may be extended to the preparation of other high-capacity porous electrodes.

Acknowledgements This work was financially supported by the National Natural Science Foundation of China (21101014, 21273022, and 51272030), the Fundamental Research Funds for the Central Universities, and the Beijing Municipal Natural Science Foundation (2112022).

References

1. Szabó DV, Kilibarda G, Schlabach S, Trouillet V, Bruns M (2012) J Mater Sci 47:4383. doi:10.1007/s10853-012-6292-7
2. Park MS, Wang GX, Kang YM, Wexler D, Dou SX, Liu HK (2007) Angew Chem Int Ed 46:750
3. Zhang YL, Liu Y, Liu ML (2006) Chem Mater 18:4643
4. Lou XW, Chen JS, Chen P, Archer LA (2009) Chem Mater 21:2868
5. Zhang L, Xiang HF, Zhu XF, Yang WS, Wang HH (2012) J Mater Sci 47:3076. doi:10.1007/s10853-011-6139-7
6. Chen LB, Yin XM, Mei L, Li CC, Lei DN, Zhang M, Li QH, Xu Z, Xu CM, Wang TH (2012) Nanotechnology 23:035402
7. Li Y, Zhu SM, Liu QL, Gu JJ, Guo ZP, Chen ZX, Feng CL, Zhang D, Moon WJ (2012) J Mater Chem 22:2766
8. Wen ZH, Wang Q, Zhang Q, Li JH (2007) Adv Funct Mater 17:2772
9. Geim AK, Novoselov KS (2007) Nat Mater 6:183
10. Novoselov KS, Geim AK, Morozov SV, Jiang D, Katsnelson MI, Grigorieva IV, Dubonos SV, Firsov AA (2005) Nature 438:197
11. Fasolino A, Los JH, Katsnelson MI (2007) Nat Mater 6:858
12. Stoller MD, Park SJ, Zhu YW, An JH, Ruoff RS (2008) Nano Lett 8:3498
13. Park MS, Wang GX, Kang YM, Wexler D, Dou SX, Liu HK (2007) Angew Chem Int Ed 46:750
14. Shiva K, Rajendra HB, Subrahmanyam KS, Bhattacharyya AJ, Rao CNR (2012) Chem Eur J 18:4489
15. Wang DH, Kou R, Choi D, Yang ZG, Nie ZM, Li J, Saraf LV, Hu DH, Zhang JG, Graff GL, Liu J, Pope MA, Aksay IA (2010) ACS Nano 4:1587
16. Yang SB, Feng XL, Ivanovici S, Müllen K (2010) Angew Chem Int Ed 49:8408
17. Chen DY, Ji G, Ma Y, Lee JY, Lu JM (2011) ACS Appl Mater Interfaces 3:3078
18. Yue WB, Xu XX, Su ZX, Irvine JTS, Zou YC, Liu YL, Zhou WZ (2012) J Mater Sci 47:2146. doi:10.1007/s10853-011-6015-5
19. Das N, Biswas PK (2012) J Mater Sci 47:289. doi:10.1007/s10853-011-5797-9
20. Lin ZZ, Yue WB, Huang DZ, Hu JY, Zhang XY, Yuan ZY, Yang XJ (2012) RSC Adv 2:1794
21. Liu H, Wang GX, Liu J, Qiao SZ, Ahn H (2011) J Mater Chem 21:3046
22. Kim H, Cho J (2008) J Mater Chem 18:771
23. Wang H, Wu YM, Bai YS, Zhou W, An YR, Li JH, Guo L (2011) J Mater Chem 21:10189
24. Yin XM, Chen LB, Li CC, Hao QY, Liu S, Li QH, Zhang ED, Wang TH (2011) Electrochim Acta 56:2358
25. Yue WB, Lin ZZ, Jiang SH, Yang XJ (2012) J Mater Chem 22:16318
26. Zhou XS, Yin YX, Wan LJ, Guo YG (2012) J Mater Chem 22:17456
27. Wilhelm P, Stephan D (2007) J Photochem Photobiol A 185:19
28. Tu YF, Fu QM, Sang JP, Zou XW (2012) J Mater Sci 47:1541. doi:10.1007/s10853-011-5944-3
29. Li D, Muller MB, Gilje S, Kaner RB, Wallace GG (2008) Nat Nanotechnol 3:101
30. Zhang JL, Yang HJ, Shen GX, Cheng P, Zhang JY, Guo SW (2010) Chem Commun 46:1112
31. Shon JK, Kong SS, Kim YS, Lee JH, Park WK, Park SC, Kim JM (2009) Microporous Mesop Mater 120:441
32. Hummers WS, Offeman RE (1958) J Am Chem Soc 80:1339
33. Chou SL, Wang JZ, Zhong C, Rahman MM, Liu HK, Dou SX (2009) Electrochim Acta 54:7519
34. Li YM, Lv XJ, Lu J, Li JH (2010) J Phys Chem C 114:21770
35. Li FH, Song JF, Yang HF, Gan SY, Zhang QX, Han DX, Ivaska A, Niu L (2009) Nanotechnology 20:455602
36. Song HJ, Zhang LC, He CL, Qu Y, Tian YF, Lv Y (2011) J Mater Chem 21:5972
37. Shang NG, Papakonstantinou P, Sharma S, Lubarsky G, Li MX, McNeill DW, Quinn AJ, Zhou WZ, Blackley R (2012) Chem Commun 48:1877
38. Ko YD, Kang JG, Park JG, Lee SJ, Kim DW (2009) Nanotechnology 20:455701
39. Zhang B, Zheng QB, Huang ZD, Oh SW, Kim JK (2011) Carbon 49:4524
40. Zhu CZ, Fang YX, Wen D, Dong SJ (2011) J Mater Chem 21:16911